

## **Supplementary Material:**

iSpa3D: An interpretable deep learning framework for 3D spatial  
domain reconstruction and domain-specific gene discovery in  
multi-slice spatial transcriptomics

## **Contents**

<b>1 Table</b>	<b>2</b>
<b>2 Figure</b>	<b>4</b>
<b>3 Supplementary Algorithm</b>	<b>20</b>

# 1 Table

Table S1: Summary of spatial transcriptomics datasets used in this study.

Platform	Tissue	Section	Spots	Genes	Reference	
10x Visium	Human dorsolateral prefrontal cortex (DLPFC)	151507	4,226	33,538	[1, 2]	
		151508	4,384			
		151509	4,789			
		151510	4,634			
		151669	3,661			
		151670	3,498			
		151671	4,110			
		151672	4,015			
		151673	3,639			
		151674	3,673			
Stereo-seq	Sagittal mouse brain (SMB)	151675	3,592	32,285	[3–5]	
		151676	3,460			
		Section 1 anterior	2,695			
		Section 1 posterior	3,355			
	Mouse embryo (ME)	Section 2 anterior	2,825			
		Section 2 posterior	3,289			
		E9.5_E1S1	5,913			
	Axolotl brain (AB)	E10.5_E2S1	8,494			
		E11.5_E1S1	30,124			
	Mouse olfactory bulb (MOB)	Control_Juv	11,698			
		Adult	8,243			
Slide-seqV2	Mouse olfactory bulb (MOB)	/	19,109	27,106	[6]	
STARmap PLUS	AD Mouse Brain (ADMB)	Mouse olfactory bulb (MOB)	/	20,139	21,220	[6]
		8 month control	8,506	2,766	[7]	
		8 month disease	8,186			
		13 month control	8,034			
MERFISH	Mouse hypothalamic preoptic (MHP)	13 month disease	10,372	155	[8, 9]	
		Bregma -0.04 mm	5,488			
		Bregma -0.09 mm	5,557			
		Bregma -0.14 mm	5,926			
		Bregma -0.19 mm	5,803			
ST	Coronal Mouse Brain (CMB)	Bregma -0.24 mm	5,543	23,371	[10, 11]	
		01A–35A	152–620			

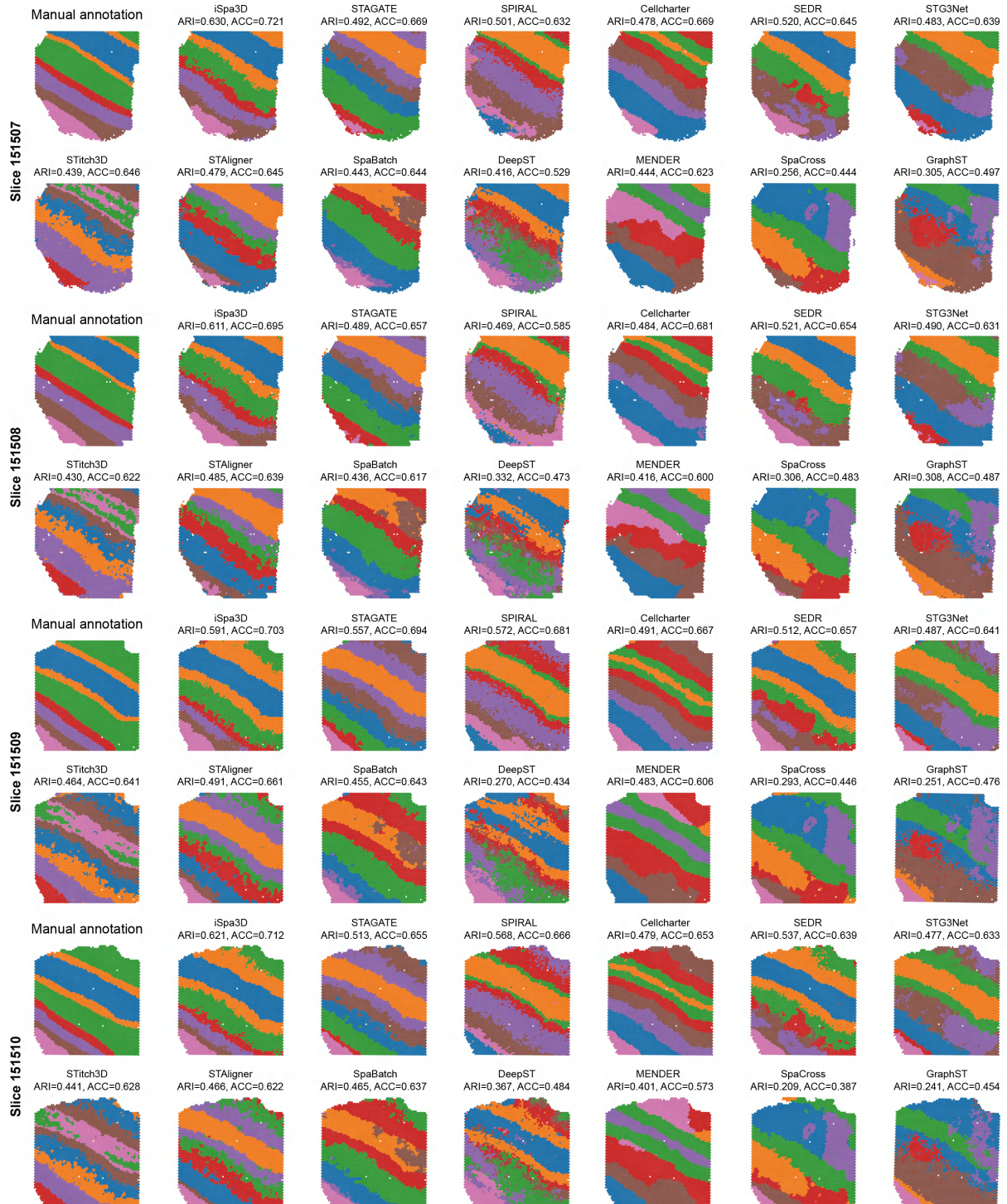
Table S2: Overview of comparative spatial domain identification methods.

Method	Methodology	Input Data	Link
STAGATE [12]	Single-slice representation learning	Spatial location data Gene expression data	<a href="#">GitHub</a>
SEDR [5]	Single-slice representation learning	Spatial location data Gene expression data	<a href="#">GitHub</a>
GraphST [13]	Single-slice representation learning	Spatial location data Gene expression data	<a href="#">GitHub</a>
DeepST [14]	Single-slice representation learning	Spatial location data Gene expression data Histology information	<a href="#">GitHub</a>
STAligner [15]	Multi-slice integration and batch correction	Spatial location data Gene expression data	<a href="#">GitHub</a>
SpaBatch [16]	Multi-slice integration and batch correction	Spatial location data Gene expression data	<a href="#">GitHub</a>
STG3Net [17]	Multi-slice integration and batch correction	Spatial location data Gene expression data	<a href="#">GitHub</a>
SPIRAL [18]	Multi-slice integration and batch correction	Spatial location data Gene expression data	<a href="#">GitHub</a>
SpaCross [19]	Multi-slice integration and batch correction	Spatial location data Gene expression data	<a href="#">GitHub</a>
STitch3D [20]	3D tissue modeling	Spatial location data Gene expression data	<a href="#">GitHub</a>
CellCharter [21]	Microenvironment discovery	Spatial location data Gene expression data	<a href="#">GitHub</a>
MENDER [22]	Microenvironment discovery	Spatial location data Gene expression data	<a href="#">GitHub</a>

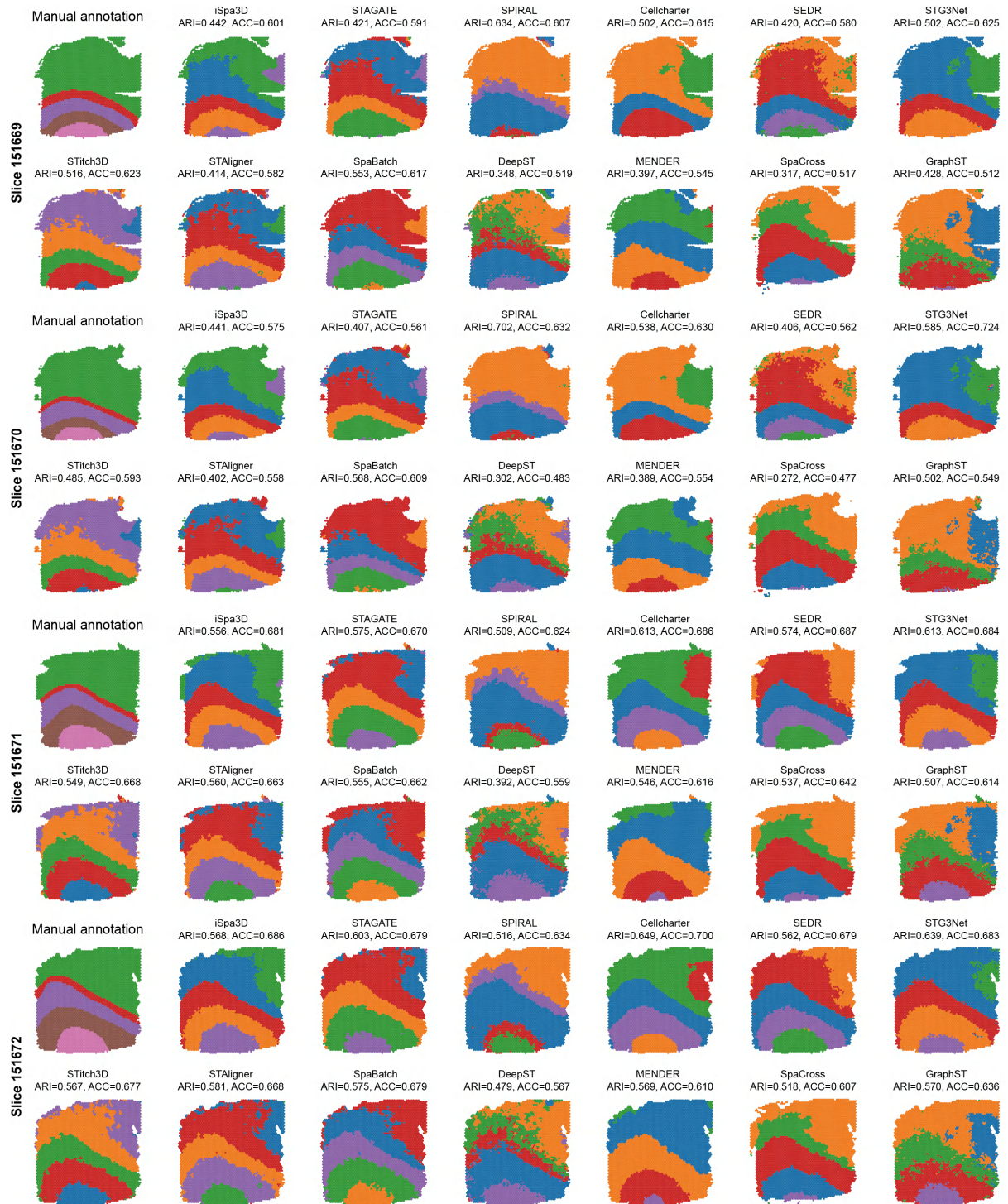
Table S3: Computational efficiency and memory consumption across datasets. MR denotes the model runtime measured as wall-clock training time. GMU represents the peak GPU memory allocated during training. MC indicates the peak GPU memory reserved by the caching allocator.

Dataset	Spots	MR (s)	GMU (MB)	MC (MB)
DLPFC_Donor_1	18,033	205.78	407.76	440.00
DLPFC_Donor_2	15,284	171.91	314.27	356.00
DLPFC_Donor_3	14,364	166.74	332.19	390.00
Mouse embryo	44,531	676.94	1,620.68	1,730.00
Sagittal_Mouse_Brain_Section1	6,050	112.97	715.51	818.00
Sagittal_Mouse_Brain_Section2	6,114	125.33	724.68	816.00
Axolotl brain	19,941	286.91	878.48	916.00
Mouse olfactory bulb	39,248	547.42	984.41	1,038.00
AD Mouse Brain	35,098	456.09	1,026.42	1,066.00
Mouse hypothalamic preoptic	28,317	461.76	607.01	646.00
Coronal Mouse Brain	17,086	308.89	676.69	710.00

## 2 Figure



See next page



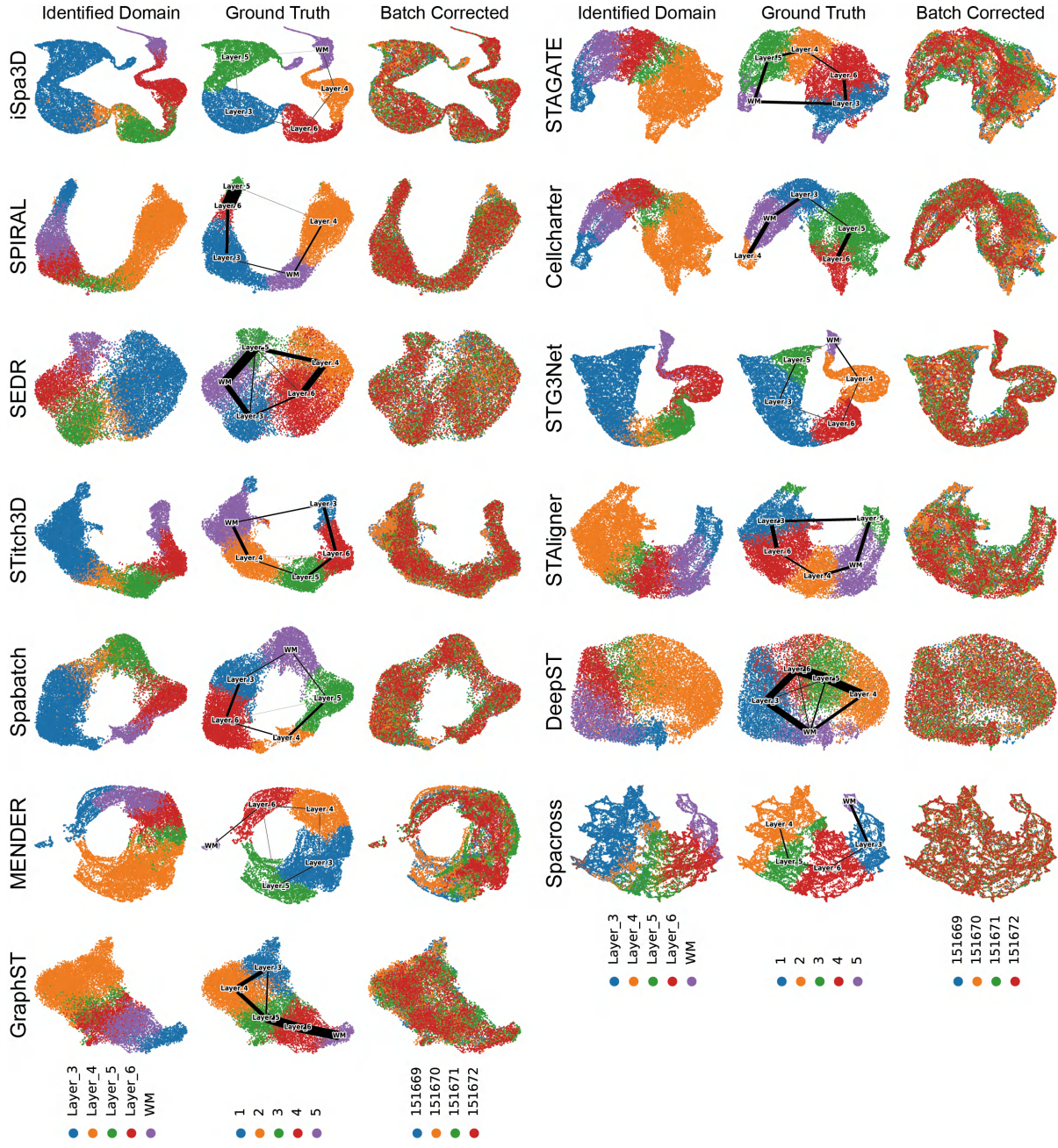
See next page



Figure S1: Comparison of spatial domains by clustering assignments via iSpa3D, various methods, and manual annotation in all 12 sections of the DLPFC dataset.



See next page



See next page

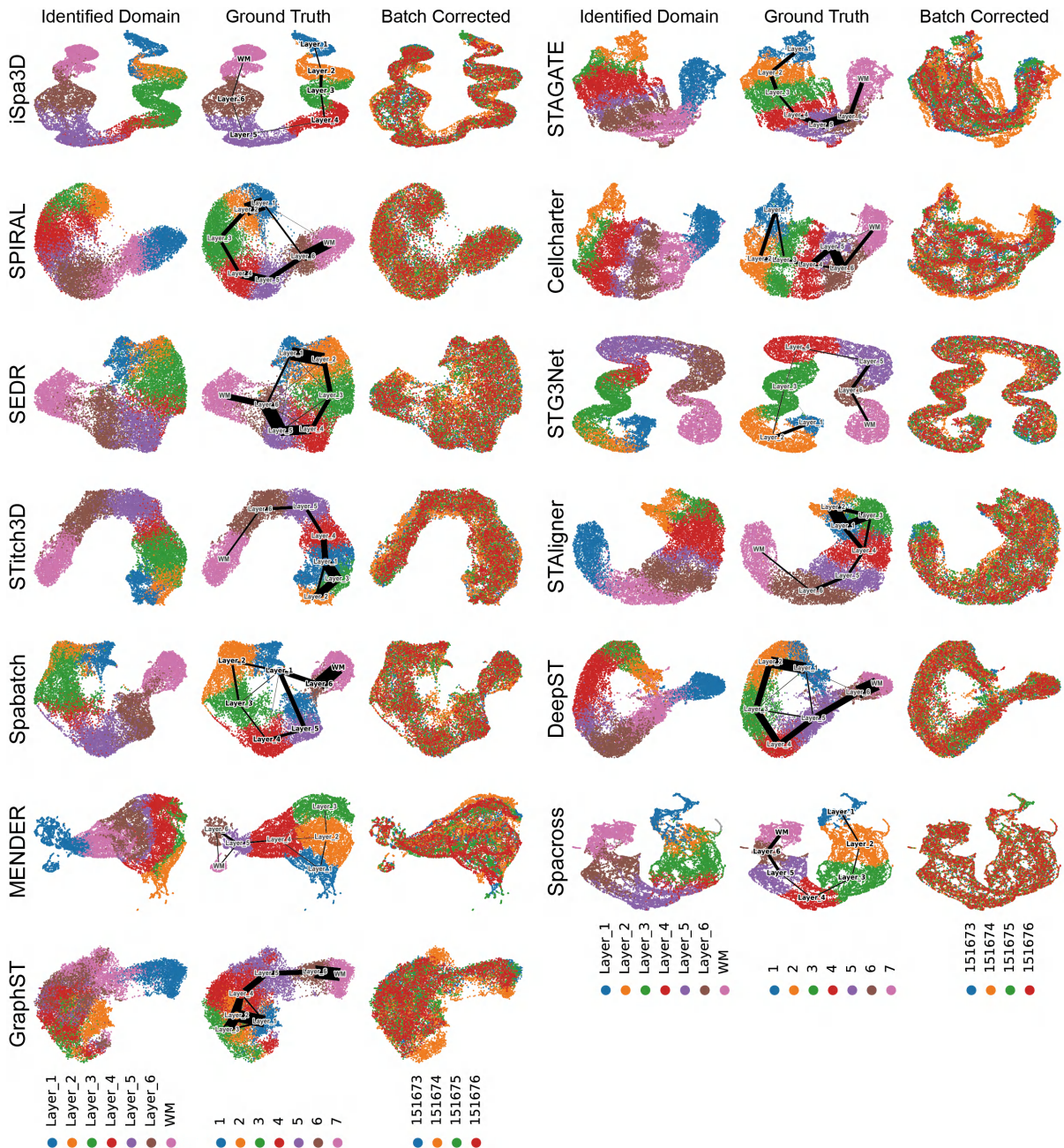


Figure S2: UMAP visualization of the embeddings from the DLPFC dataset, colored by identified spatial domains (left), ground truth (middle), and batch-corrected results (right).

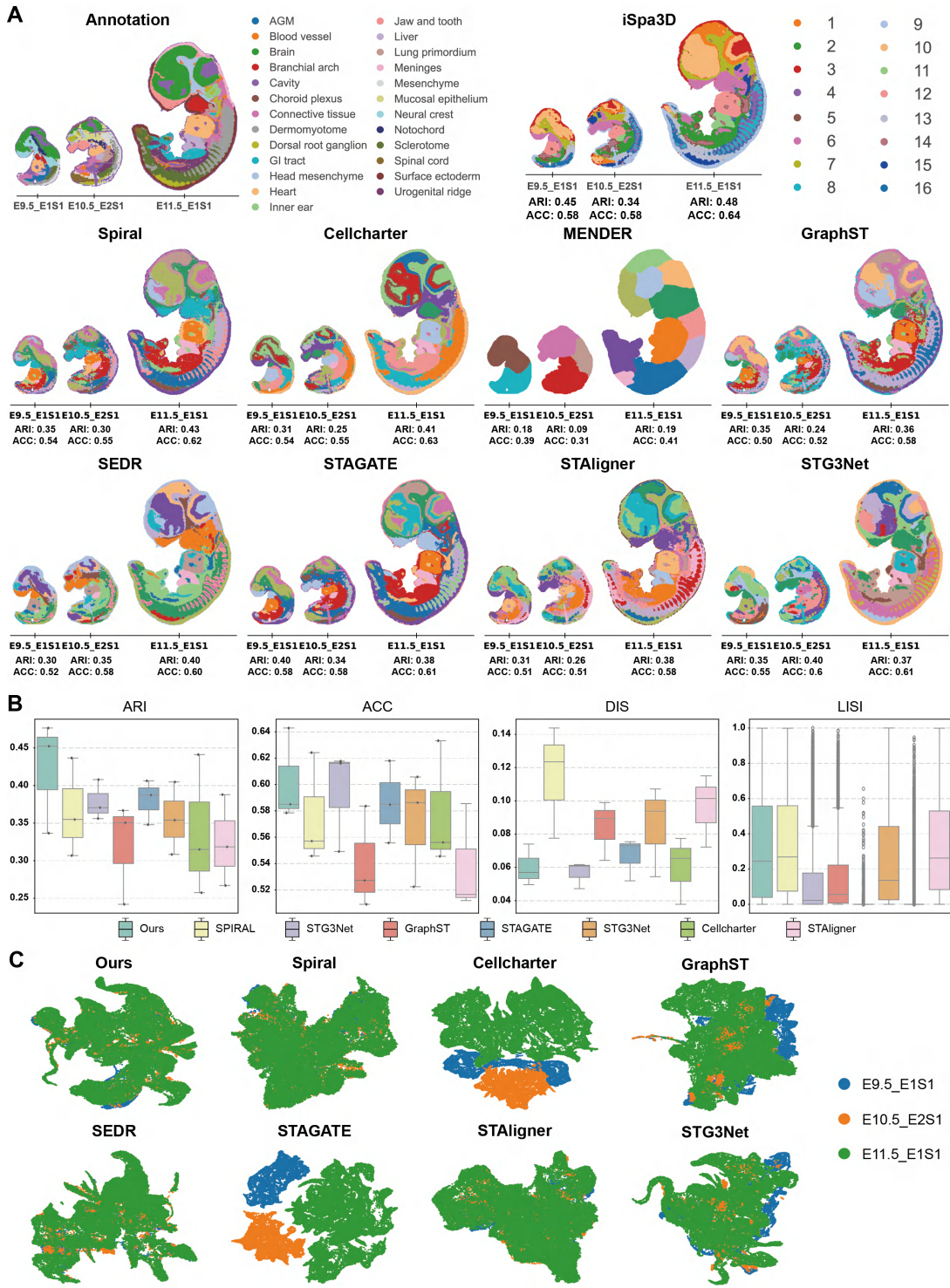


Figure S3: Evaluation of cross-stage spatial domain identification and batch integration on the mouse embryo dataset. **(A)** The top panel displays the ground truth anatomical annotations alongside the spatial domains identified by iSpa3D across three developmental stages (E9.5, E10.5, and E11.5), with corresponding ARI and ACC scores. The lower panels present the spatial clustering results of eight baseline methods for visual benchmarking against the ground truth. **(B)** Boxplots illustrate the statistical comparison of iSpa3D (Ours) against baseline methods across four key metrics. **(C)** Low-dimensional latent representations of spots from all three developmental stages are visualized via UMAP and colored by Stage. This visualization demonstrates the effectiveness of iSpa3D and competing methods in aligning datasets across different temporal batches while preserving biological structures.

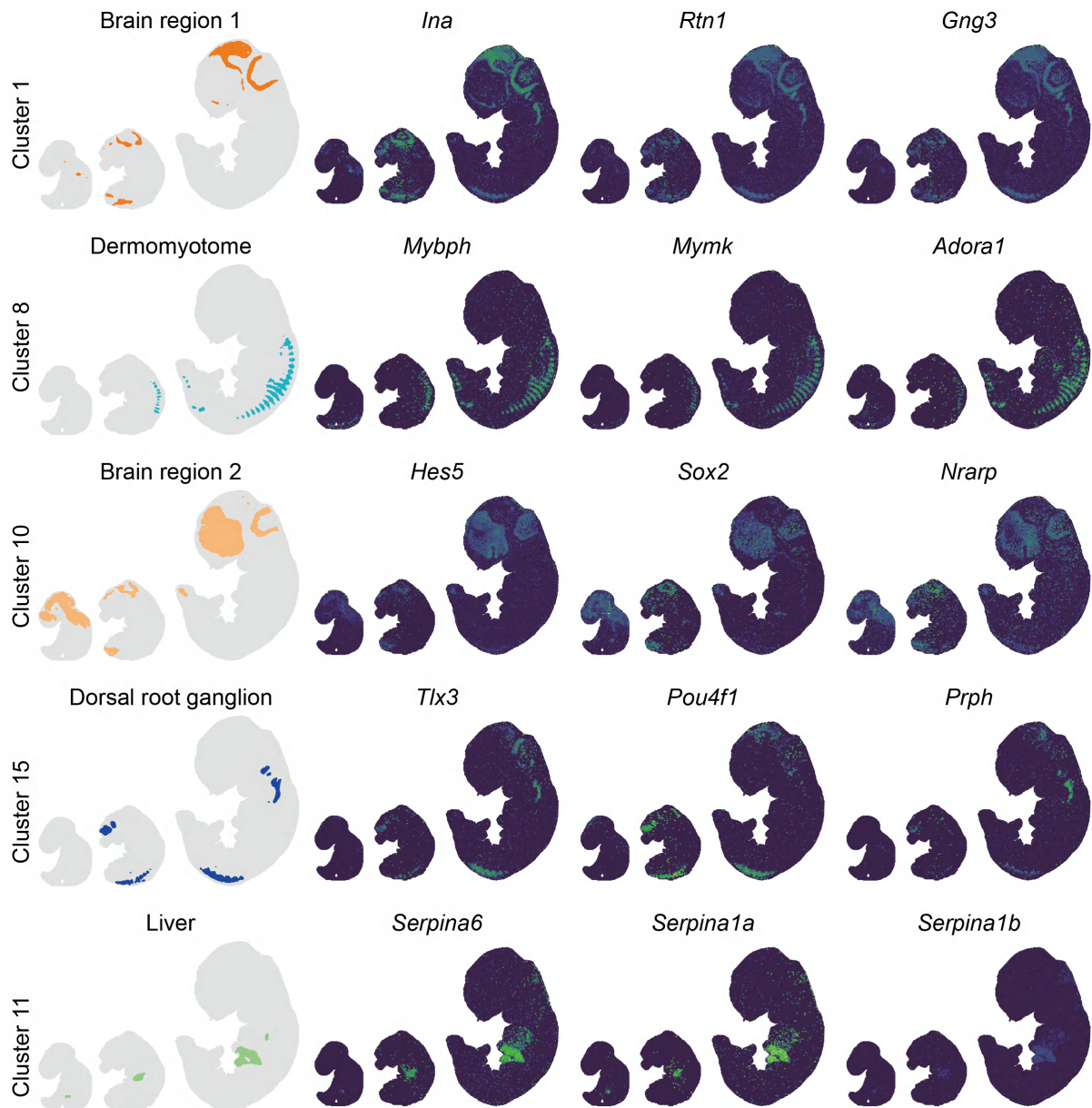


Figure S4: Visualization of domain-specific spatially variable genes (SVGs) identified by the iSpa3D interpretability module in the mouse embryo. Each row corresponds to a distinct spatial domain identified by the model. The leftmost column displays the spatial distribution of the specific cluster across three developmental stages (E9.5, E10.5, and E11.5). The subsequent columns present the spatial expression heatmaps of representative top-10-ranked marker genes prioritized by the interpretability module for that specific domain.

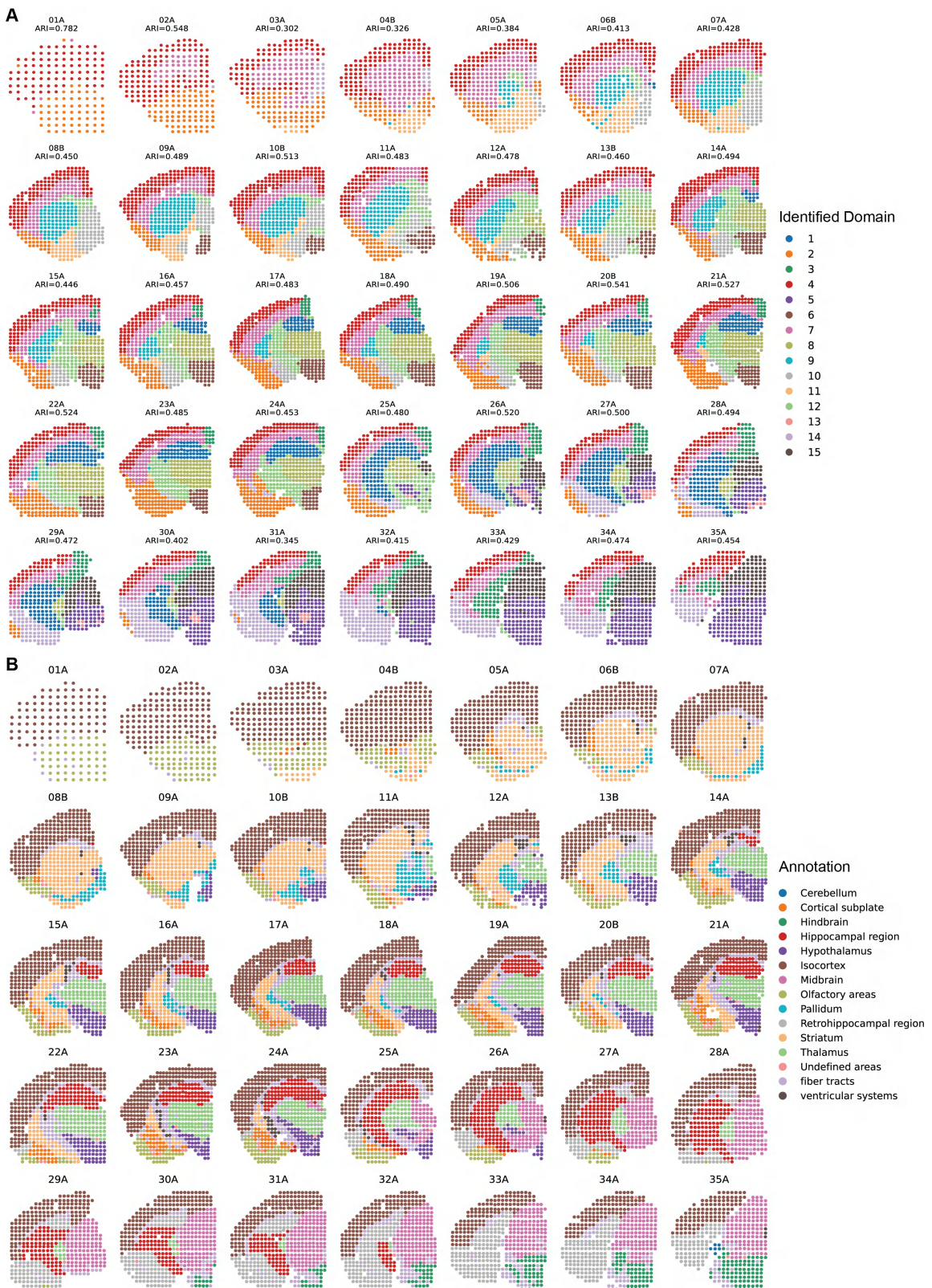


Figure S5: (A) iSpa3D spatial domain identification results.(B) Manual annotation of mouse brain data from 35 slices.

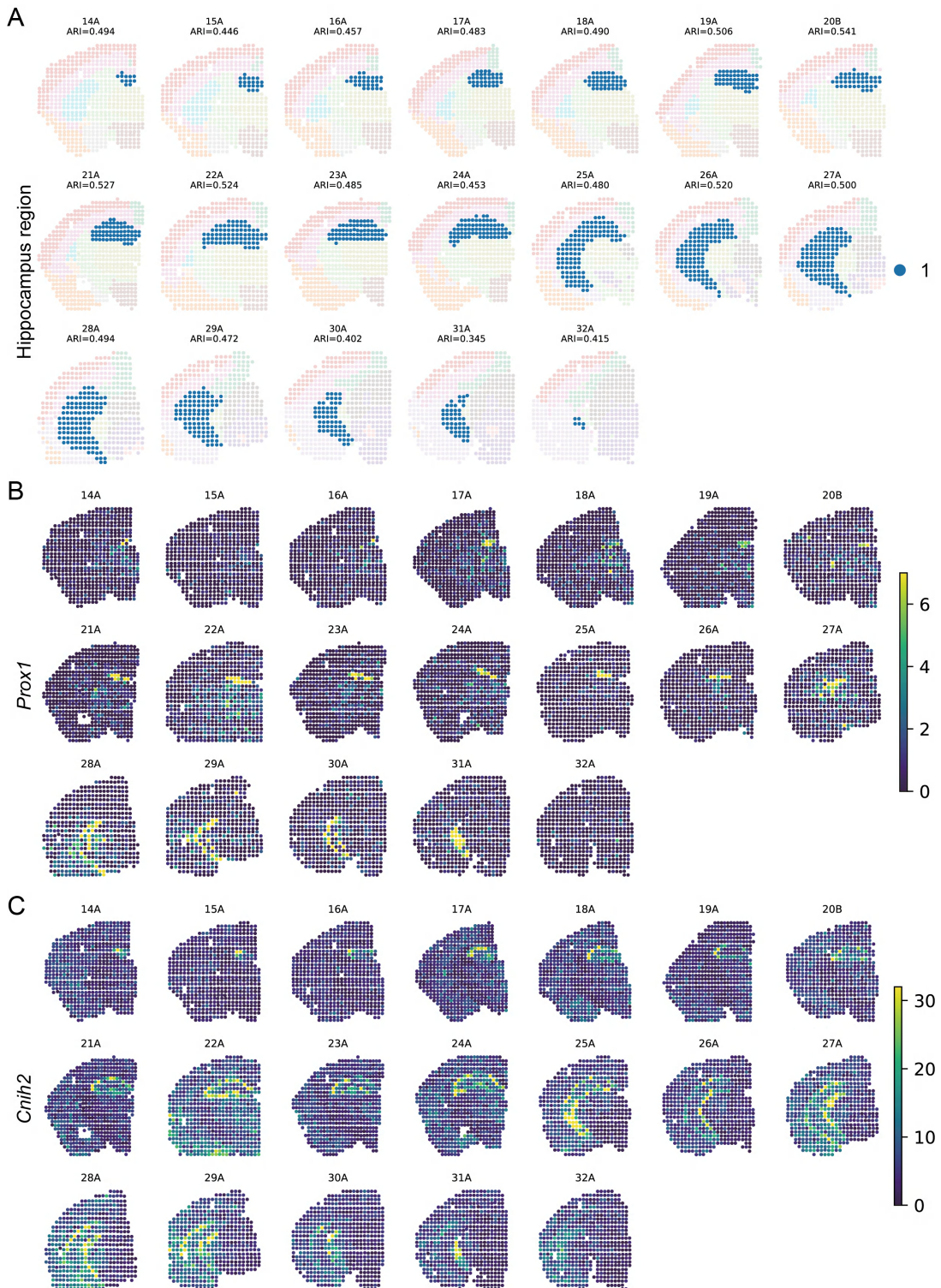


Figure S6: Visualization of the iSpa3D-identified hippocampus region and SVGs detected by the interpretability module in the mouse brain. **(A)** The spatial distribution of the identified hippocampus region (Cluster 1) across continuous coronal sections (from 14A to 32A), spanning from its emergence to disappearance. Blue dots represent spots assigned to the hippocampus domain by iSpa3D. The ARI for each slice is indicated above the corresponding section. **(B–C)** Spatial expression heatmaps of representative top-ranked spatially variable genes (SVGs) identified by the interpretability module for the hippocampus domain, visualized using raw gene expression levels. The spatial expression patterns of *Prox1* and *Cnih2* exhibit strong enrichment within the hippocampal region, aligning precisely with the identified spatial domain.

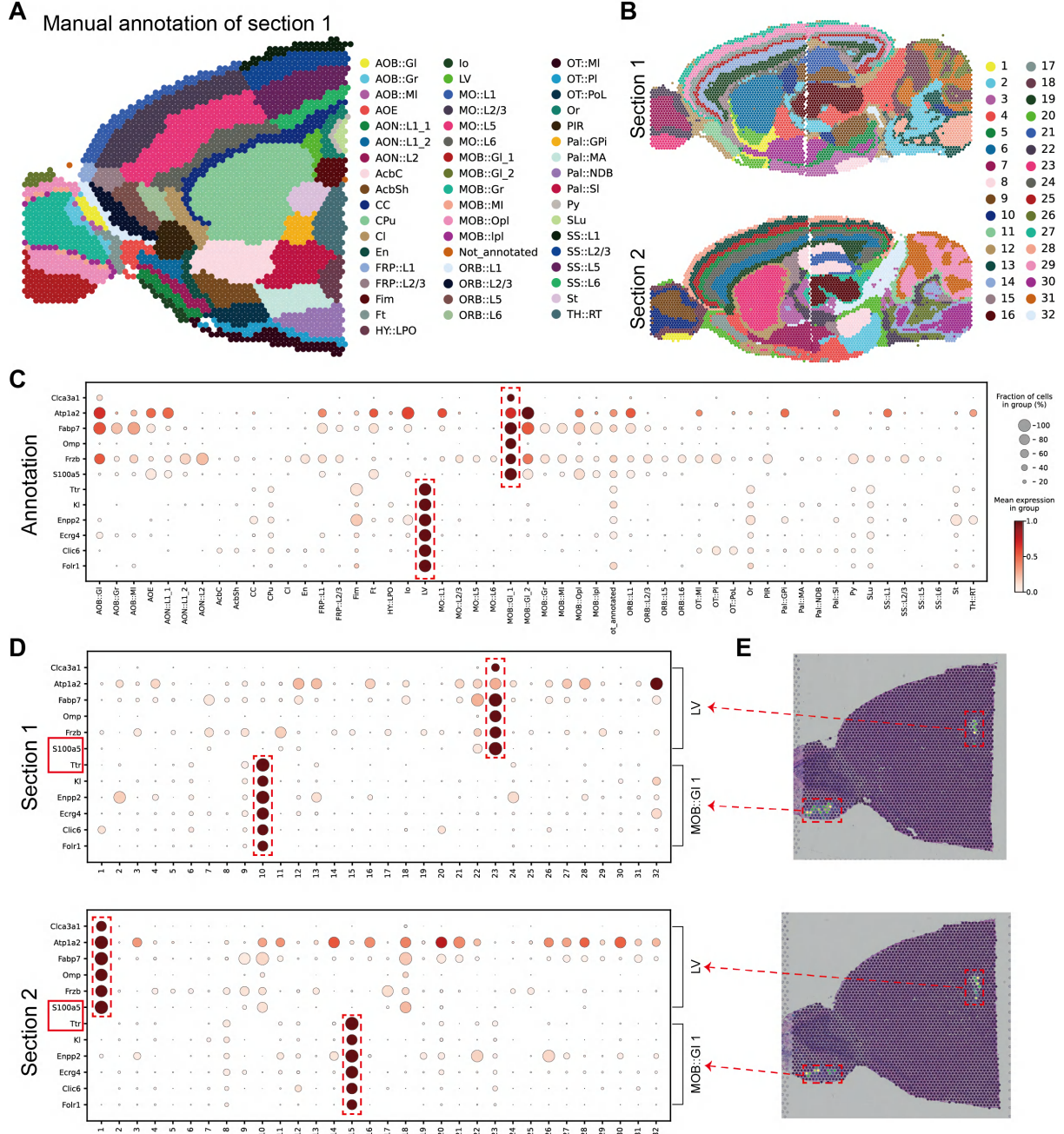


Figure S7: Stitching and fine-grained subdomain identification in mouse brain sagittal sections using iSpa3D. **(A)** Manual annotation of the anterior part of Section 1. **(B)** Integration results of Section 1 and Section 2 using iSpa3D, showing a coherent spatial domain map across the stitched sections. **(C)** Dot plot showing the expression of marker genes across manually annotated anatomical regions, serving as the ground truth reference. **(D)** Dot plots of representative top-ranked spatially variable genes (SVGs) identified by the interpretability module for specific spatial domains in Section 1 and Section 2. The expression patterns in the identified clusters (highlighted in red boxes) align well with the manually annotated spatial domains, specifically the Main Olfactory Bulb Glomerular layer (MOB::GI) and Lateral Ventricle (LV). **(E)** Visualization of the raw gene expression levels for the marker genes *S100a5* and *Ttr*.

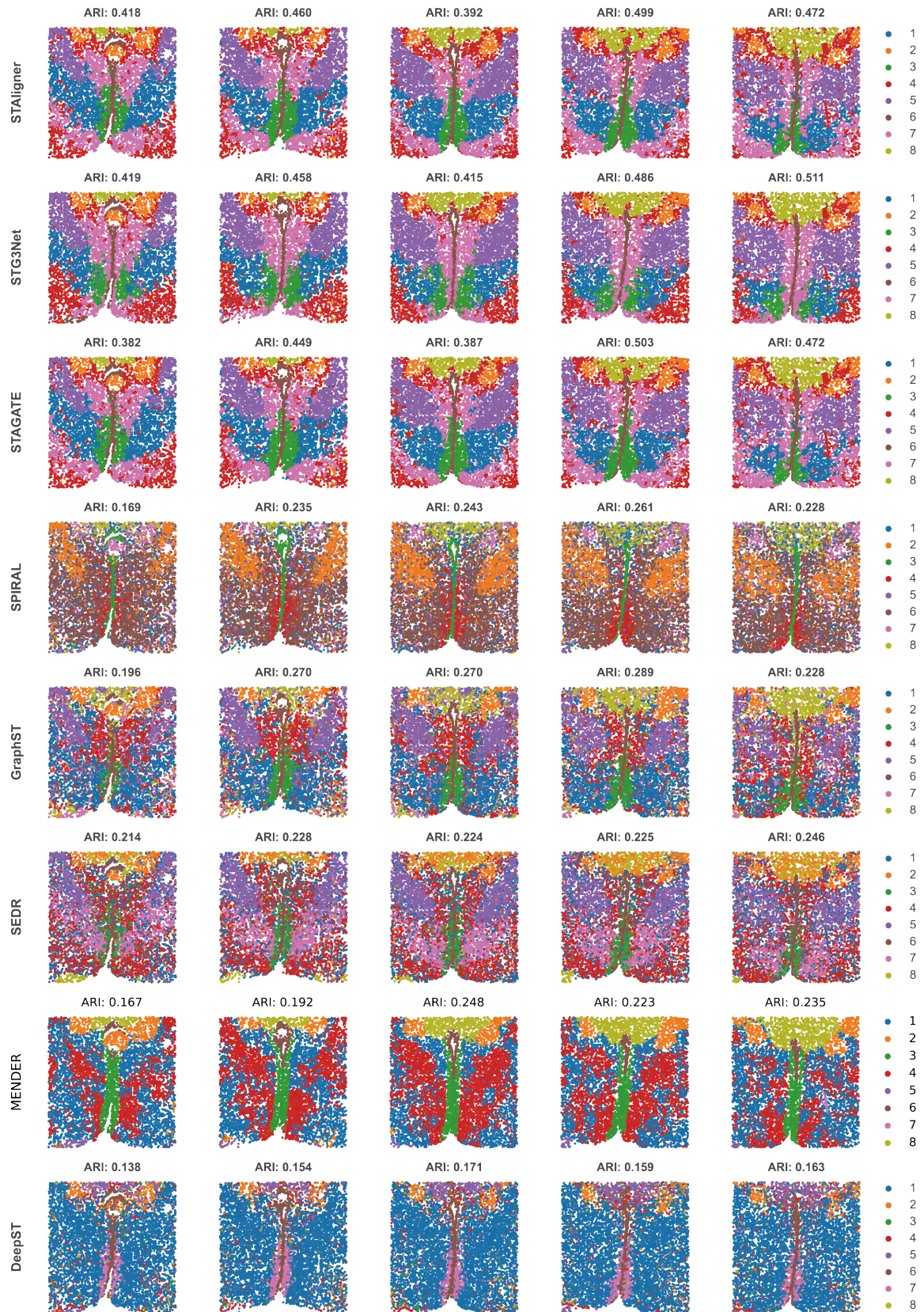


Figure S8: Spatial domains detected by STAligner, STG3Net, STAGATE, SPIRAL, GraphST, SEDR, MENDER and DeepST on the mouse hypothalamus from the MERFISH platform

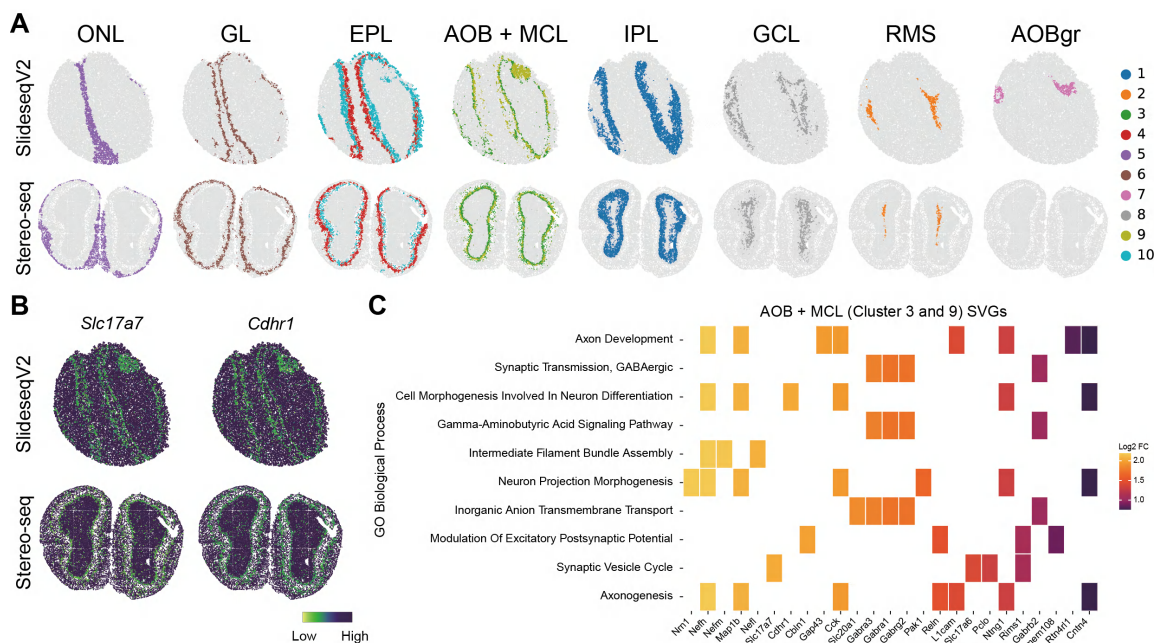


Figure S9: (A) Visualization of the spatial distributions of distinct morphological layers identified by iSpa3D across two different platforms: Slide-seqV2 (top row) and Stereo-seq (bottom row). Columns represent specific anatomical regions, including the Olfactory Nerve Layer (ONL), Glomerular Layer (GL), External Plexiform Layer (EPL), Accessory Olfactory Bulb and Mitral Cell Layer (AOB + MCL), Internal Plexiform Layer (IPL), Granule Cell Layer (GCL), Rostral Migratory Stream (RMS), and the fine-grained Accessory Olfactory Bulb granular layer (AOBgr). (B) Spatial expression heatmaps of two representative marker genes, *Slc17a7* and *Cdhr1*. (C) GO enrichment analysis of the domain-specific spatially variable genes (SVGs) identified by the interpretability module for the AOB and MCL regions (Clusters 3 and 9).

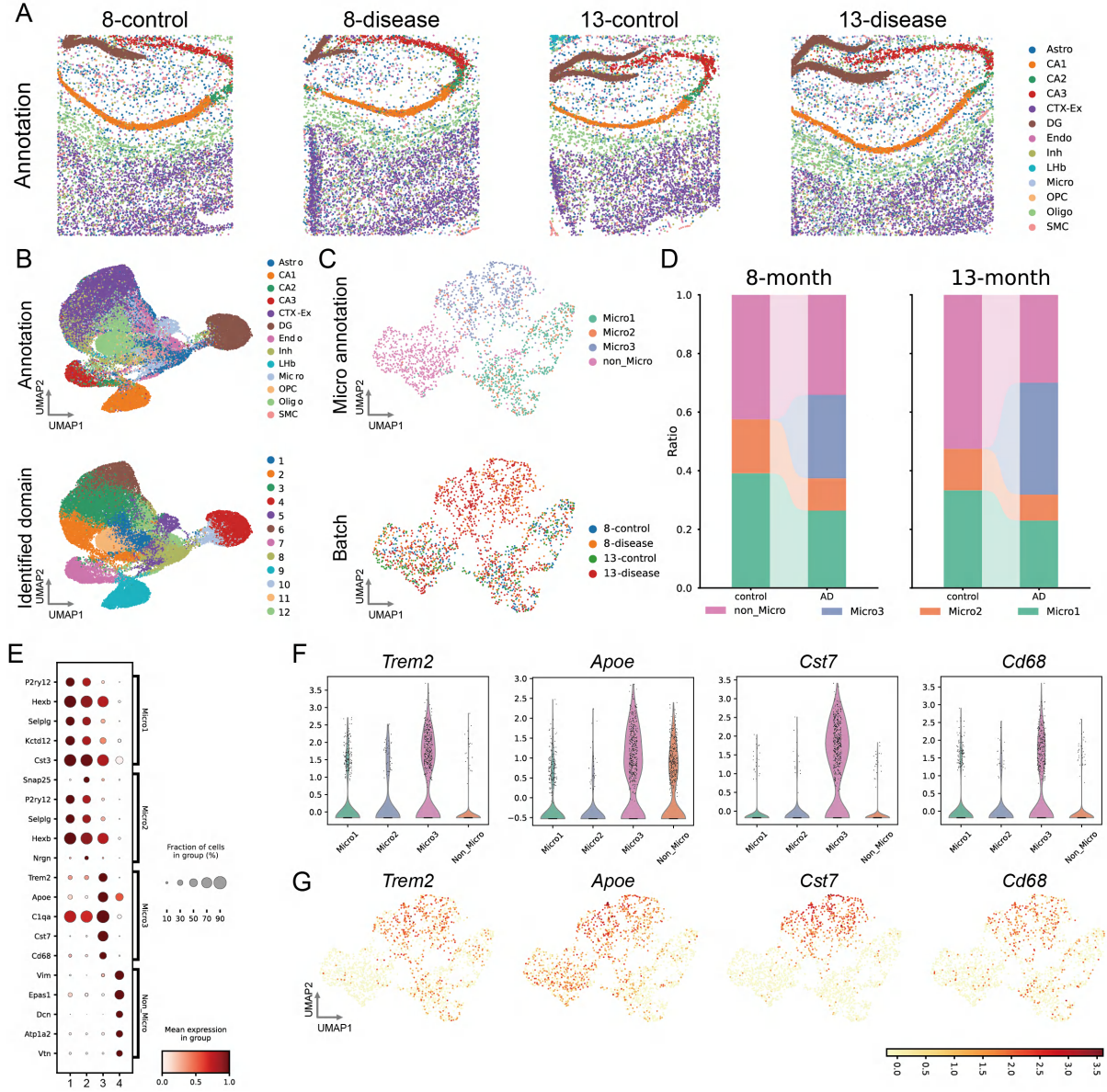


Figure S10: Characterization of disease-associated microglia sub-populations in the Alzheimer's disease (AD) mouse model via iSpa3D domain sub-clustering. **(A)** Spatial distribution of manually annotated cell types across four brain sections representing different disease stages (8 and 13 months) and conditions (Control and Disease). **(B)** UMAP visualization of all single cells colored by manual annotations (top) and iSpa3D-identified spatial domains (bottom), revealing that Domain 5 corresponds to the microglia/immune population. **(C)** Sub-clustering analysis of the cells within iSpa3D-identified Domain 5. The UMAPs display three distinct microglia subtypes (Micro1, Micro2, Micro3) and a non-microglia cluster (top), alongside the batch distribution (bottom). **(D)** Stacked bar plots quantifying the cellular composition of the sub-clusters across different groups. Notably, the Micro3 population exhibits a substantial expansion in the AD (Disease) samples compared to Controls at both time points, suggesting a disease-reactive state. **(E)** Dot plot showing the top differentially expressed genes for each sub-cluster. **(F)** Violin plots and **(G)** feature plots demonstrate that genes such as *Trem2*, *Apoe*, *Cst7*, and *Cd68* are highly enriched in the Micro3 cluster, confirming its identity as a pathology-associated microglial population.

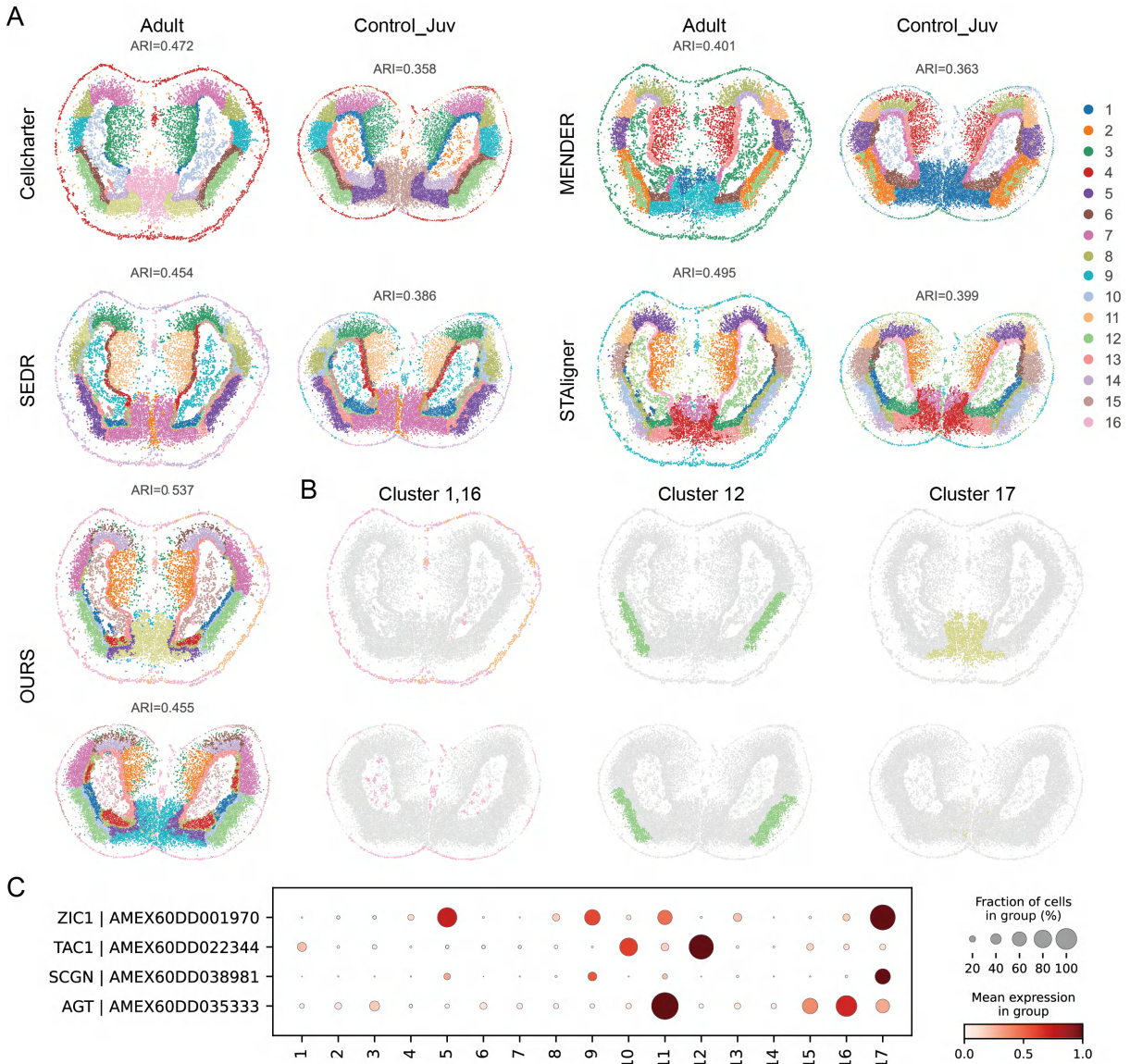
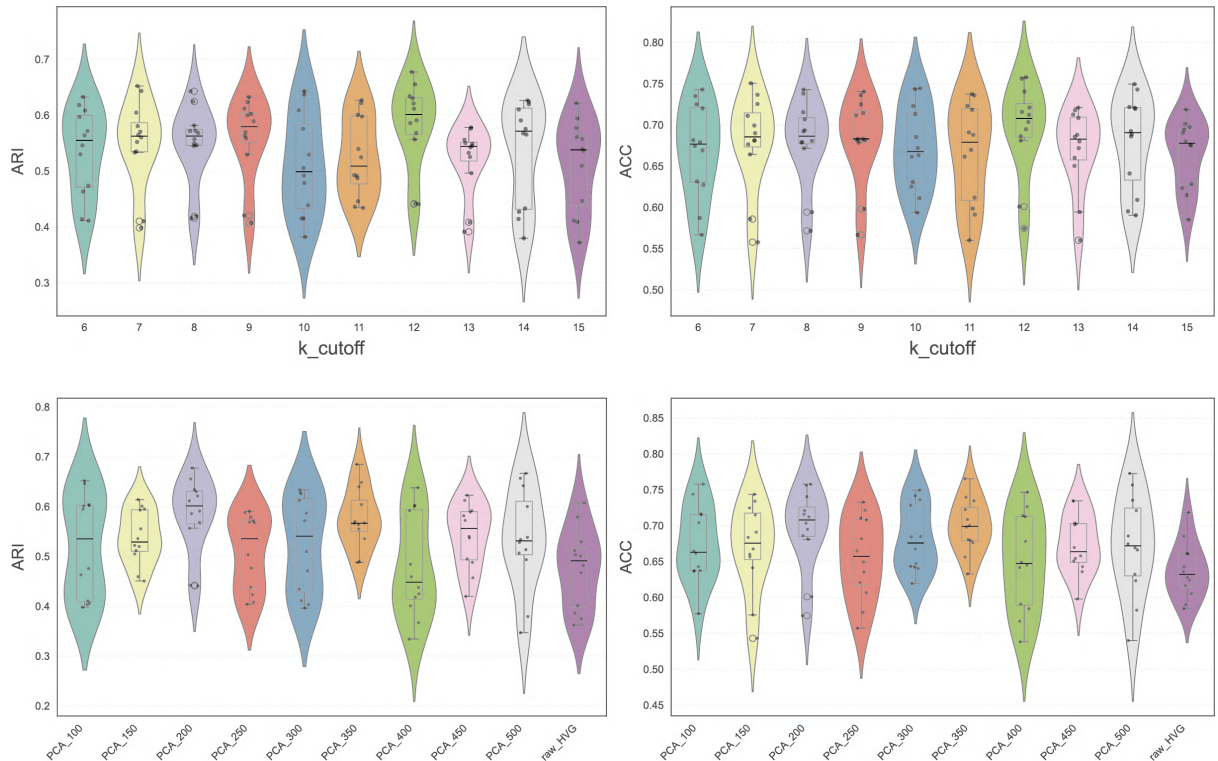


Figure S11: **(A)** Comparison of spatial clustering results between iSpa3D (OURS) and the four methods (Cellcharter, MENDER, SEDR, and STAligner) across Adult and Juvenile developmental stages. The ARI is provided for each method. **(B)** Visualization of specific spatial domains identified by iSpa3D (Clusters 1 & 16, Cluster 12, and Cluster 17). **(C)** Dot plot displaying the expression intensity and fraction of top-ranked domain-specific spatially variable genes (SVGs) identified by the interpretability module. Representative markers, such as *TAC1* (highly specific to the striatum-like Cluster 12) and *AGT* (enriched in Cluster 17), align with the spatial regions highlighted in **(B)**.



**Figure S12:** **(Top)** Clustering performance (ARI and ACC) of iSpa3D across 12 DLPFC slices as the number of neighbors in spatial graph construction ( $k_{\text{cutoff}}$ ) varies from 6 to 15. The model exhibits robust performance, with optimal results observed at 12 neighbors. **(Bottom)** ARI and ACC scores under varying PCA dimensionality (ranging from 100 to 500) and a baseline using raw highly variable genes (raw\_HVG). The best performance is consistently achieved with 200 PCA components.

### 3 Supplementary Algorithm

---

**Algorithm 1** iSpa3D: 3D Spatial Domain Identification via Self-supervised Learning

---

**Input:** Multi-slice gene expression matrices  $\{\mathbf{X}^{(s)}\}_{s=1}^S$ , spatial location matrices  $\{\mathbf{P}^{(s)}\}_{s=1}^S$ , masking rate  $\rho$ , pre-training epochs  $T_p$ , graph encoder  $F_g$ , graph decoder  $G_d$ , discriminator  $D$ , number of clusters  $K$

**Output:** 3D spatial domain labels

```

1: // Data Preprocessing and Graph Construction
2: Concatenate gene expression matrices across slices
3: Filter low-quality genes, normalize counts, select highly variable genes
4: Apply PCA to obtain feature matrix  $\mathbf{X} \in \mathbb{R}^{N \times m}$  where  $m = 200$ 
5: Construct  $k$ -NN spatial graph for each slice
6: Assemble block-diagonal adjacency matrix  $\mathbf{A}$  and apply normalization
7: // Pre-training Phase
8: for  $t = 0$  to  $T_p - 1$  do
9:   // Complementary Masking
10:  Generate random permutation and partition spots into  $V_{\text{mask}}$  and  $V_{\text{keep}}$ 
11:  Construct complementary masked views  $\tilde{\mathbf{X}}^{(1)}$  and  $\tilde{\mathbf{X}}^{(2)}$ 
12:  // Encoder-Decoder Forward Pass
13:  Encode both views:  $\mathbf{Z}^{(1)} \leftarrow F_g(\tilde{\mathbf{X}}^{(1)}, \tilde{\mathbf{A}})$ ,  $\mathbf{Z}^{(2)} \leftarrow F_g(\tilde{\mathbf{X}}^{(2)}, \tilde{\mathbf{A}})$ 
14:  Decode both views:  $\hat{\mathbf{X}}^{(1)} \leftarrow G_d(\tilde{\mathbf{A}}, \mathbf{Z}^{(1)})$ ,  $\hat{\mathbf{X}}^{(2)} \leftarrow G_d(\tilde{\mathbf{A}}, \mathbf{Z}^{(2)})$ 
15:  // Loss Computation
16:  Compute Scaled Cosine Error loss  $\mathcal{L}_{\text{rec}}$  on masked spots
17:  if  $t \geq T_{\text{warmup}}$  then
18:    Compute cluster assignments via contrastive head
19:    Calculate cluster-level InfoNCE loss  $\mathcal{L}_{\text{proto}}$ 
20:    Compute marginal distribution regularization  $\mathcal{L}_{\text{margin}}$ 
21:     $\mathcal{L}_{\text{clu}} \leftarrow \mathcal{L}_{\text{proto}} + \mathcal{L}_{\text{margin}}$ 
22:  else
23:     $\mathcal{L}_{\text{clu}} \leftarrow 0$ 
24:  end if
25:  if  $t \bmod 50 = 0$  then
26:    Identify MNN pairs across slices and construct triplet tuples  $\mathcal{T}$ 
27:  end if
28:  Compute triplet margin loss  $\mathcal{L}_{\text{tri}}$ 
29:  // Adversarial Training
30:  D-step: Update discriminator  $D$  to maximize batch classification accuracy
31:  G-step: Update encoder  $F_g$  with reversed gradient to confuse discriminator
32:  Compute total loss  $\mathcal{L}_{\text{total}} = \lambda_1 \mathcal{L}_{\text{rec}} + \lambda_2 \mathcal{L}_{\text{tri}} + \lambda_3 \mathcal{L}_{\text{disc}} + \lambda_4 \mathcal{L}_{\text{clu}}$ 
33:  Update encoder and decoder parameters via gradient descent
34: end for
35: // 3D Spatial Reconstruction
36: Compute final latent embeddings  $\mathbf{Z}$  from encoder
37: for each pair of adjacent slices do
38:  Identify MNN anchor pairs in latent space
39:  Compute optimal rigid transformation via SVD
40:  Apply transformation to align slices
41: end for
42: Stack aligned slices into 3D coordinates
43: Perform clustering on 3D latent embeddings
44: return 3D spatial domain labels

```

---

---

**Algorithm 2** iSpa3D: Domain-specific SVG Discovery via Differential Attribution

---

**Input:** Gene expression matrix  $\mathbf{X}$ , spatial graph  $\tilde{\mathbf{A}}$ , pre-trained encoder  $F_g$ , spatial domain labels from Algorithm 1, fine-tuning epochs  $T_f$

**Output:** Domain-specific spatially variable genes (SVGs)

```
1: // Fine-tuning Phase: Supervised Domain Classification
2: Initialize MLP classifier  $f_{\text{MLP}}$  for spatial domain prediction
3: for  $t = 0$  to  $T_f - 1$  do
4:   Forward pass:  $\mathbf{Z} \leftarrow F_g(\mathbf{X}, \tilde{\mathbf{A}})$  (allow encoder fine-tuning)
5:   Predict domain labels:  $\hat{\mathbf{Y}} \leftarrow f_{\text{MLP}}(\mathbf{Z})$ 
6:   Compute cross-entropy loss and update parameters via backpropagation
7: end for
8: // Differential Attribution Module
9: for each spatial domain  $c$  do
10:  Define spatial neighborhood  $\text{NBR}(c)$  using radius  $R$  and threshold  $\tau$ 
11:  Construct baseline set  $\mathcal{B}_c$  from neighbor domain centroids
12:  for each attribution method  $\mathcal{M} \in \{\mathcal{IG}, \mathcal{OC}, \mathcal{GS}\}$  do
13:    for each spot  $i$  in domain  $c$  do
14:      Compute gene-level attribution vector  $\mathcal{W}_i^{\mathcal{M}}$  targeting logit  $S_c(\mathbf{x}_i)$ 
15:      Apply  $\ell_2$  normalization to attribution vectors
16:    end for
17:    Compute mean attribution for domain  $c$  and its neighbors
18:    Compute domain-differential scores:  $\Delta_{c,j}^{\mathcal{M}} = \hat{\mathcal{W}}_{c,j}^{\mathcal{M}} - \hat{\mathcal{W}}_{\text{nbr}(c),j}^{\mathcal{M}}$ 
19:    Rank genes by differential scores to obtain  $r_{c,j}^{\mathcal{M}}$ 
20:  end for
21:  // Consensus Ranking via Borda Count
22:  Aggregate rankings:  $\text{Score}_{c,j} = \sum_{\mathcal{M}} (m + 1 - r_{c,j}^{\mathcal{M}})$ 
23:  Sort genes by  $\text{Score}_{c,j}$  in descending order
24:  Select top- $K$  genes or apply adaptive threshold  $\hat{\mu} + \lambda\hat{\sigma}$ 
25: end for
26: return Domain-specific SVGs for each 3D spatial domain
```

---

## References

- [1] Andrew L Ji, Adam J Rubin, et al. Multimodal analysis of composition and spatial architecture in human squamous cell carcinoma. *Cell*, 182(2):497–514, 2020.
- [2] Kristen R Maynard, Leonardo Collado-Torres, et al. Transcriptome-scale spatial gene expression in the human dorsolateral prefrontal cortex. *Nature Neuroscience*, 24(3):425–436, 2021.
- [3] Ao Chen, Sha Liao, et al. Spatiotemporal transcriptomic atlas of mouse organogenesis using dna nanoball-patterned arrays. *Cell*, 185(10):1777–1792, 2022.
- [4] Xiaoyu Wei, Sulei Fu, Hanbo Li, Yang Liu, Shuai Wang, Weimin Feng, Yunzhi Yang, Xiawei Liu, Yan-Yun Zeng, Mengnan Cheng, et al. Single-cell stereo-seq reveals induced progenitor cells involved in axolotl brain regeneration. *Science*, 377(6610):eabp9444, 2022.
- [5] Hang Xu, Huazhu Fu, et al. SEDR: Unsupervised spatially embedded deep representation of spatial transcriptomics. *Genome Medicine*, 16(1):1–15, 2024.
- [6] Robert R Stickels, Evan Murray, et al. Highly sensitive spatial transcriptomics at near-cellular resolution with slide-seqv2. *Nature Biotechnology*, 39(3):313–319, 2021.
- [7] Hu Zeng, Jiahao Huang, Haowen Zhou, William J Meilandt, Borislav Dejanovic, Yiming Zhou, Christopher J Bohlen, Seung-Hye Lee, Jingyi Ren, Albert Liu, et al. Integrative in situ mapping of single-cell transcriptional states and tissue histopathology in a mouse model of alzheimer’s disease. *Nature neuroscience*, 26(3):430–446, 2023.
- [8] Kok Hao Chen, Alistair N Boettiger, et al. Spatially resolved, highly multiplexed rna profiling in single cells. *Science*, 348(6233):aaa6090, 2015.
- [9] Jeffrey R Moffitt, Dhananjay Bambah-Mukku, et al. Molecular, spatial, and functional single-cell profiling of the hypothalamic preoptic region. *Science*, 362(6416):eaau5324, 2018.
- [10] Patrik L Ståhl, Fredrik Salmén, Sanja Vickovic, Anna Lundmark, José Fernández Navarro, Jens Magnusson, Stefania Giacomello, Michaela Asp, Jakub O Westholm, Mikael Huss, et al. Visualization and analysis of gene expression in tissue sections by spatial transcriptomics. *Science*, 353(6294):78–82, 2016.
- [11] Vitalii Kleshchevnikov, Artem Shmatko, et al. Cell2location maps fine-grained cell types in spatial transcriptomics. *Nature Biotechnology*, 40(5):661–671, 2022.
- [12] Kangning Dong and Shihua Zhang. STAGATE: Deciphering spatial domains from spatially resolved transcriptomics with an adaptive graph attention auto-encoder. *Nature Communications*, 13(1):1739, 2022.

- [13] Yahui Long, Kok Siong Ang, et al. GraphST: Spatially informed clustering, integration, and deconvolution of spatial transcriptomics with graphst. *Nature Communications*, 14(1):1155, 2023.
- [14] Chang Xu, Xiyun Jin, et al. DeepST: identifying spatial domains in spatial transcriptomics by deep learning. *Nucleic Acids Research*, 50(22):e131–e131, 2022.
- [15] Xiang Zhou, Kangning Dong, et al. Integrating spatial transcriptomics data across different conditions, technologies and developmental stages. *Nature Computational Science*, 3(10):894–906, 2023.
- [16] Jinyun Niu, Donghai Fang, Jinyu Chen, Yi Xiong, Juan Liu, and Wenwen Min. Spabatch: Deep learning-based cross-slice integration and 3d spatial domain identification in spatial transcriptomics. *Advanced Science*, page e09090, 2025.
- [17] Donghai Fang, Fangfang Zhu, et al. Multi-slice spatial transcriptomics data integration analysis with stg3net. In *2024 IEEE International Conference on Bioinformatics and Biomedicine (BIBM)*, pages 509–514. IEEE, 2024.
- [18] Tiantian Guo, Zhiyuan Yuan, et al. Spiral: integrating and aligning spatially resolved transcriptomics data across different experiments, conditions, and technologies. *Genome Biology*, 24(1):241, 2023.
- [19] Donghai Fang and Wenwen Min. Spacross deciphers spatial structures and corrects batch effects in multi-slice spatially resolved transcriptomics. *Communications Biology*, 8(1):1393, 2025.
- [20] G. Wang, J. Zhao, Y. Yan, et al. Construction of a 3D whole organism spatial atlas by joint modelling of multiple slices with deep neural networks. *Nature Machine Intelligence*, 5(11):1200–1213, 2023.
- [21] Marco Varrone, Daniele Tavernari, Albert Santamaria-Martínez, Logan A Walsh, and Giovanni Ciriello. Cellcharter reveals spatial cell niches associated with tissue remodeling and cell plasticity. *Nature genetics*, 56(1):74–84, 2024.
- [22] Zhiyuan Yuan. Mender: fast and scalable tissue structure identification in spatial omics data. *Nature Communications*, 15(1):207, 2024.